Detailed characterisation of an indoor MIMO channel in the double directional spatial domain

M. Matthaiou   D.I. Laurenson   J.S. Thompson

Institute for Digital Communications, Joint Research Institute for Signal and Image Processing, School of Engineering and Electronics, The University of Edinburgh, King's Buildings, Edinburgh EH9 3JL, UK
E-mail: M.Matthaiou@ed.ac.uk

Abstract: The spatial domain characteristics of an indoor multiple-input multiple-output (MIMO) communication system are examined in detail. Using a high-resolution algorithm, the authors were able to effectively estimate multipath parameters on the joint azimuth of arrival/azimuth of departure (AoA/AoD) domain. The analysis showed dense clustering phenomena at the vast majority of considered locations and a strong correlation between the azimuth spreads of the two angular domains with the presence of line-of-sight (Los) specular components or when the distance between the transmitter (Tx) and the receiver (Rx) is low. The authors also noticed higher azimuth dispersions, compared with those reported in the literature, which can be attributed to low antenna heights and local scattering interactions in the vicinity of both the transmit and receive arrays. Finally, the impact of the spatial global parameters on the ergodic MIMO capacity was tested revealing a direct relation between them.

1   Introduction

It is well established that the use of multiple antenna elements at both ends of a radio link can result in remarkably high spectral efficiencies for supporting future demanding wireless applications [1]. This is achieved by the exploitation of the surrounding multipath environment that generates multiple spatial subchannels which in turn are able to convey multiple data streams between the transmitter (Tx) and the receiver (Rx). More interestingly, the characterisation and modelling of multiple-input multiple-output (MIMO) systems have triggered an extensive research interest over the recent years since an accurate model can, in principle, predict the propagation mechanisms and ultimately make possible the integration of MIMO technology into practical systems.

For MIMO characterisation, a detailed knowledge of the statistical distributions of the multipath parameters is essential. This usually involves extensive real-time measurement campaigns followed by joint extraction of the propagation characteristics in different signal domains, these are, time of arrival (ToA), azimuth of arrival (AoA),

azimuth of departure (AoD), complex path gain etc. This can be accomplished by the use of multidimensional high-resolution estimation algorithms which are applied directly to the raw measurement data [2, 3]. The major contributions of this paper on channel characterisation as well as the relation to previous and concurrent work can now be summarised as follows:

• Firstly, an efficient and robust frequency domain (FD) version of the space-alternating generalised expectation-maximisation (SAGE) array processing algorithm to extract the paths' parameters of a realistic indoor MIMO channel is introduced. The obtained estimates are thereafter used to assess the channel performance in both angular domains by means of clustering, dispersion and statistical correlation.

• Given that the data post-processing disclosed that multipath components (MPCs) tend to gather into clusters in the joint AoA/AoD domain, we are particularly interested in the so-called intercluster or global parameters as defined in the European Cooperation in Scientific and Technical 273 (COST 273) research initiative [4]. Henceforth, we define clusters as an accumulation of

MPCs with similar angular characteristics, i.e., AoAs and AoDs. The formation of clusters in the temporal domain was initially studied by Saleh and Valenzuela (SV) [5], which concluded that this phenomenon is caused by the superstructure of the environment. The SV model was later extended into the spatial domain for single-input single-output (SISO) and dynamic single-input multiple-output (SIMO) channels by Spencer *et al.* [6] and Chong *et al.* [7], respectively. In the present contribution, we introduce a flexible technique for identifying clusters in the joint AoA/AoD domain, namely a kernel density estimate (KDE). Using the same set of data as in this paper, the authors in [8] proposed a hard decision scheme for identifying clusters which, however, may result in an overestimation of the true number of clusters.

• We also investigate the azimuth dispersion properties of both angular domains and the degree of correlation between them; the first comprehensive study of azimuth dispersion can be found in [9] and its extension in [10]. The authors considered different outdoor scenarios and examined the level of temporal and azimuth dispersion as well as the degree of correlation between them. Similar work was also reported in [11–13]. However, all these studies were limited to the joint spatio-temporal dispersion and therefore disregarded the spatial activity at the transmit side. What's more, the authors in [6] assumed that the spatial and temporal domains are independent while the authors in [7] demonstrated that this assumption is invalid for line-of-sight (LoS) scenarios; in such an environment paths arriving at the Rx with short delays have a relatively large angular spread whereas paths arriving with longer delays have angles very similar to the LoS direction, thereby leading to a dependency between the two domains. We will show that a similar conclusion can be drawn for the double directional domain as well. Recently, the dispersion experienced at the Tx in an outdoor-to-indoor channel was addressed but the authors focused on the intra-cluster (within clusters) properties which implies that the formulation of a broader channel description was beyond their scope [14].

The paper is organised as follows: In Section 2, an indoor MIMO measurement campaign is described while in Section 3, a high-resolution algorithm for extracting the paths' parameters is outlined. The procedure for identifying clusters in the AoA/AoD domain is discussed in Section 4. In Section 5, the dispersion experienced at both azimuth domains is addressed along with the degree of correlation between them as well as the effects of global spatial parameters on MIMO capacity. Finally, Section 6 concludes the paper.

2 Indoor measurement campaign

An indoor measurement campaign was carried out in the Electrical Engineering Building (Vienna University of Technology) in a highly cluttered environment. The kernel of the measurement setup was the RUSK ATM MEDAV vector channel sounder which operated at a centre frequency of 5.2 GHz [15]. The sounder was probed at 193 equi-spaced frequency bins covering the 120 MHz of operating bandwidth with a dynamic range of typically 35 dB. The two ends were synchronised via an optical fibre [16, 17]. The measurements were repeated over 128 temporal snapshots in order to enhance the output signal-to-noise ratio (SNR). Evidently, the channel should be static during one such snapshot and for this reason the campaign was conducted at night to ensure stationarity. By averaging over all snapshots, the receive SNR was increased by $10 \cdot \log(128) = 21$ dB theoretically to values up to $55-60$ dB; we note, however, that the signal discrimination remains limited by the dynamic range of the sounder [17].

The Rx was mounted on a wooden tripod at a height of 1.5 m and employed a uniform linear array (ULA) of eight vertically-polarised printed dipoles with an inter-element distance of 0.4λ. Two dummy elements were also used. Each single antenna had a 3 dB beamwidth of about $120°$. Prior to any AoA estimation process, the physical receive array must be fully calibrated in order to remove the undesired effects of electromagnetic mutual coupling between the antenna elements, amplification errors, non-identical element responses and other array imperfections. For this reason the effects of mutual coupling were mitigated using the method described in [18]. At the Tx, an omni-directional sleeve antenna was moved on a 10×20 rectangular grid with element spacings of 0.5λ. By considering a virtual eight-element ULA on each row, we end up with $13 \times 10 = 130$ spatial realisations of the 8×8 MIMO transfer matrix. Hence, a total set of $130 \times 193 = 25{,}090$ space and frequency realisations per measurement scenario was obtained.

For this study, 24 different Rx locations were investigated in several offices while the Tx was positioned at a fixed position in the hallway. In order to capture the whole azimuth domain activity, the Rx was steered to three different broadside directions (spaced by $120°$), leading to the generation of 72 data sets, that is, combinations of Rx positions and directions. Most office rooms were sparsely furnished with wooden and metal furniture (computers, chairs, tables). The doors between the hallway and the rooms, as well as their frames, were also wooden or glass-filled [17]. The measurement layout, along with the Rx locations, is illustrated in Fig. 1.

3 Estimation of paths' parameters: the SAGE algorithm

For the computation of the multipath parameters, the authors have recently developed a FD version of the SAGE algorithm which yields a good robustness and rapid convergence even in the presence of closely separated components [19]. Moreover, the scheme requires no spatial smoothing for mitigating the effects of correlated sources and can be applied to any arbitrary antenna geometry provided that the array manifold is fully available. Following [8], we firstly select
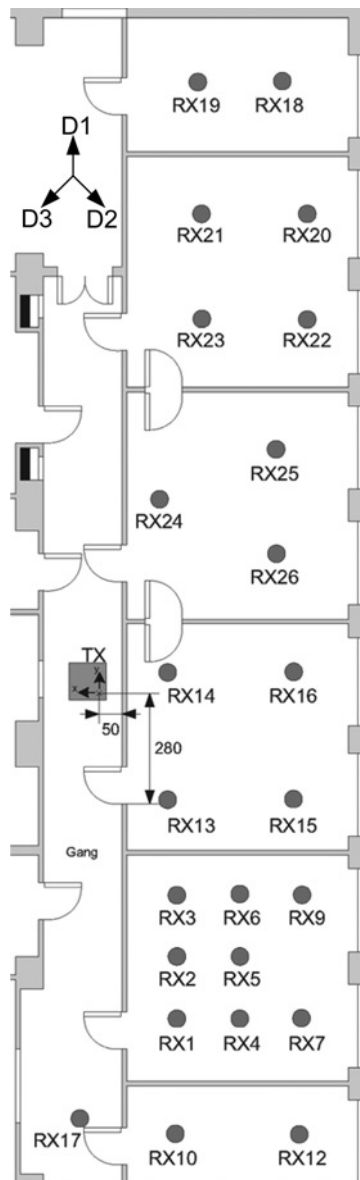
206

IET Microw. Antennas Propag., 2009, Vol. 3, Iss. 2, pp. 205–213

Figure 1 *Layout of the measurement environment along with the Rx locations*

$P = 150$ random realizations (out of the total ensemble of 25,090 realisations) of the measured 8×8 channel matrix $\boldsymbol{H}$; at the pth realisation ($p = 1, 2, \ldots, 150$), the channel matrix $\boldsymbol{H}^p$ can be expressed as the superposition of L impinging wavefronts. (This value of p not only allows a fair comparison with the results presented in [8] but also is found to satisfy the tradeoff between a low computational burden and a sufficiently large subset of the data ensemble. Besides, we verified that a further increase of P does not lead to dramatic changes in the final estimation results). The assumption of a finite number of plane wavefronts is valid as long as all signal sources as well as the scatterers are located in the corresponding far field regions. We can then write

$$\boldsymbol{H}^p = \sum_{\ell=1}^{L} \boldsymbol{S}^p(\theta_\ell) = \sum_{\ell=1}^{L} \beta_\ell^p \boldsymbol{a}(\phi_{r,\ell}^p) \boldsymbol{d}^{\mathrm{T}}(\phi_{t,\ell}^p) \quad (1)$$

where $\{\phi_{r,\ell}\}$, $\{\phi_{t,\ell}\}$ and $\{\beta_\ell\}$ denote the AoA, AoD and complex amplitude of the ℓth wave, respectively; the calibrated receive and transmit steering vectors are expressed as $\boldsymbol{a}(\phi_r)$ and $\boldsymbol{d}(\phi_t)$ while $[\cdot]^{\mathrm{T}}$ is the transposition operation. For clarity, we have concatenated all the path parameters into a vector $\theta_\ell \triangleq [\phi_{r,\ell}, \phi_{t,\ell}, \beta_\ell]$ and will also drop the realisation index p throughout the rest of the paper. Moreover, the term $\boldsymbol{S}(\theta_\ell)$ reflects the contribution of the ℓth path to the total channel transfer function response and also contains the spatial characteristics of each path. We point out that the delay resolution of 8.3 ns allows a very limited path separation (i.e. path length difference equals 2.49 m) in the delay domain and therefore we merely focus on the joint AoA/AoD domain.

By introducing the notions of expectation step (E-step) and maximisation step (M-step), the FD-SAGE algorithm can be decomposed into two sequential procedures. The estimated contribution of the ℓth wave $\hat{\boldsymbol{X}}_\ell(\hat{\vec{\theta}})$ is calculated during the E-step as

$$\hat{\boldsymbol{X}}_\ell(\hat{\vec{\theta}}) = \boldsymbol{H} - \sum_{\ell'=1}^{\ell-1} \boldsymbol{S}(\hat{\vec{\theta}}_{\ell'}) \quad (2)$$

Referring back to the original paper introducing the SAGE algorithm [20], we can readily identify $\hat{\boldsymbol{X}}_\ell(\hat{\vec{\theta}})$ as the so-called complete (unobservable) data whereas $\boldsymbol{H}$ as the so-called incomplete (observable) data. We underline the fact that in the SAGE context, the mapping from complete to incomplete data is allowed to be random rather than deterministic as occurs within the expectation maximisation (EM) algorithm. The above equation relies on a serial interference cancellation (SIC) scheme which, as was first shown in [21], yields a faster convergence rate and a more accurate performance than the parallel interference cancellation (PIC) technique in the frequency domain. The main concept of the SIC technique is to order the waves with respect to their received power in a descending order. Under these conditions, we remove the interference caused by the strong MPCs which may likely lead to inaccurate estimates of low power MPCs. In indoor environments where the multipath activity is high, due to the increased number of scatterers, the PIC scheme can be unstable and diverge from the solution, especially in low SNR scenarios. Furthermore, the PIC scheme is laborious since it requires the whole set of waves in order to compute the updated estimates.

The coordinate wise updating procedure for obtaining the parameters θ'' of each wave based on all previous estimates θ' is referred to as the M-step and expressed as

$$\hat{\phi}_{r,\ell}'' = \arg\max_{\phi_r} \left\{ \left| z(\phi_r, \hat{\phi}_{t,\ell}'; \hat{\boldsymbol{X}}_\ell(\hat{\vec{\theta}})) \right|^2 \right\} \quad (3a)$$

$$\hat{\phi}_{t,\ell}'' = \arg\max_{\phi_t} \left\{ \left| z(\hat{\phi}_{r,\ell}'', \phi_t; \hat{\boldsymbol{X}}_\ell(\hat{\vec{\theta}})) \right|^2 \right\} \quad (3b)$$

$$\hat{\beta}_{\ell}'' = \frac{1}{MN} \cdot z\left(\hat{\phi}_{r,\ell}'', \hat{\phi}_{t,\ell}''; \hat{X}_{\ell}(\hat{\theta})\right) \qquad (3c)$$

where $M = N = 8$ are the numbers of receive and transmit antenna elements. The term $z(\phi_r, \phi_t; X)$ is the so-called cost (or correlation) function; in general, the cost function originates from the fundamental concept of maximum-likelihood techniques while at each optimisation stage its peak corresponds to the expected parameter value [20]. In the present case, it is given by

$$z(\phi_r, \phi_t; X_{\ell}) \triangleq a^{\mathrm{H}}(\phi_r)X_{\ell}d^*(\phi_t) \qquad (4)$$

with $[\cdot]^{\mathrm{H}}$ and $[\cdot]^*$ being the Hermitian transposition and conjugate operations, respectively. The execution of this update process once defines one iteration cycle of the FD-SAGE algorithm. The parameter estimates are sequentially and cyclically updated until convergence is attained. The complex amplitude is then computed as the output signal normalised by the total energy. As for any other iteration method, the algorithm converges when the difference between two successive estimates becomes smaller than a predefined threshold; we have typically used a threshold of $0.1°$ as a sufficiently small iteration steps. A crucial issue in signal-estimation algorithms is the determination of the number of waves L impinging on the receiving array that are above the noise floor. Taking into account that no a priori knowledge of this number is available in real-time measurements, the SIC technique was employed until the signal's power becomes smaller than -20 dB relative to the strongest peak, which is well within the measured SNR level, so that all dominant MPCs in the received signal could be extracted.

4 Cluster identification

The next step involved cluster identification on the joint AoA/AoD spatial domain based on the SAGE estimates. Unfortunately, the widely used clustering algorithms require that the number of clusters be specified by the user which is inappropriate in the considered case [22]. Following [7], we have resorted to the use of non-parametric KDEs, which are flexible and robust, for jointly identifying the clusters. In general, KDE techniques are employed for associating a smooth non-parametric estimate of the unknown probability density function (pdf) with an arbitrary collection of observations. The KDE used throughout our analysis has been built upon a bivariate Gaussian kernel function while the two-dimensional bandwidth selection relies on a so-called direct-plug-in (DPI) method, originally proposed in [23], which yields an optimal asymptotic performance among all the related schemes. We note that a further analysis of the KDE concept is beyond the scope of this paper but the interested readers are referred to [24] for an excellent review of the most frequently used KDE techniques.

During the data post-processing, we observed a relatively low value for the number of estimated paths in the FD-SAGE algorithm for a considerable percentage of the 150 channel realisations that were analysed; on these grounds, the input parameters to the KDE were the 1000 AoA/AoD pairs, taken from the 150 channel realisations, which exhibit the largest gain amplitudes. The software implementation of KDE was obtained from [25]. It should be remembered that the weaker components may have negligible influence on the calculation of statistical spreads but can introduce unavoidable errors when calculating pdfs such as for the number of clusters. In order to get an understanding of the identification process, a scatter plot showing the joint AoA/AoD SAGE estimates is depicted in Fig. 2 (location 24D2). The corresponding joint density plot after being processed by the 2D-KDE technique can be seen in Fig. 3 with the circles corresponding to the identified clusters. We observe that clusters become far more obvious after the KDE procedure and can be easily determined by visual inspection. The estimated number of clusters is tabulated in Table 1 (columns 2-4); a mean number of 6.875 is found in our study compared to 8.8 with [8]. This difference can be attributed to the constraint of no overlapping clusters imposed by the authors therein which is relaxed in the present work. This limitation may generally lead to an overestimation of the number of clusters since in realistic channels, clusters are not always clearly separated and therefore they likely can overlap.

5 Global parameters of the spatial domains

In this section, a deeper insight in the spatial domain characteristics is provided. We firstly evaluate the dispersive nature of both spatial domains with a view to their root mean squared (rms) azimuth spread; subsequently, we assess the degree of double directional inter-dependency by means of the correlation coefficient which is the most
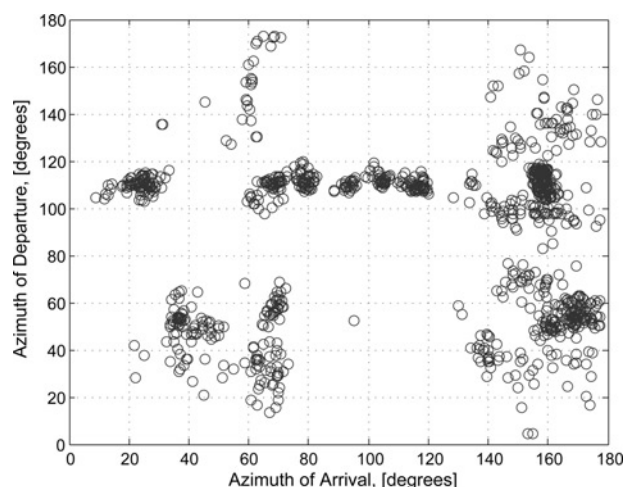

Figure 2 *Scatter plot of MPCs AoA-AoD as obtained from the SAGE algorithm (location 24D2)*
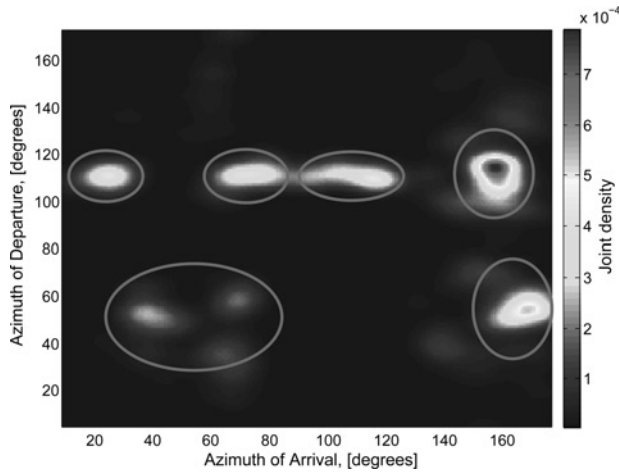
Figure 3 *Joint density distribution after being processed by the 2D KDE with the circles showing the identified clusters (location 24D2)*

common statistical figure of merit. The ergodic capacity variations as a function of all global parameters are presented in the last part of this section.

5.1 Angular dispersion

It is widely known that the beneficial effects of MIMO technology can be severely limited by spatial correlation at both ends of the radio link, that is the signal correlation between the antenna elements [26]. The degree of spatial correlation is inversely related to the spatial dispersion usually characterised by the rms azimuth spread, or the root second central moment of the power azimuth spectrum (PAS)

$$\phi_{t,rms} = \sqrt{\frac{\sum_{\ell=1}^{L} P_{\phi_t}(\ell) \cdot \phi_t(\ell)^2}{\sum_{\ell=1}^{L} P_{\phi_t}(\ell)} - \frac{\left(\sum_{\ell=1}^{L} P_{\phi_t}(\ell) \cdot \phi_t(\ell)\right)^2}{\left(\sum_{\ell=1}^{L} P_{\phi_t}(\ell)\right)^2}} \tag{5}$$

where $P_{\phi_t}(\ell)$ is the power of the ℓth MPC in the transmit PAS. The same notation holds for the receive side. Given the vital importance of both azimuth spreads, we have evaluated them on each of the 150 random realisations. The obtained cumulative distribution functions (cdfs) for a LoS (17D1) and an non-LoS (NLoS) (16D2) location can be seen in Figs. 4 and 5, respectively. A lognormal distribution is fitted to the empirical data and plotted for comparison since it was found that it yields an accurate match for the great majority of the considered scenarios. This implies that the azimuth spread can be directly described by the density

$$f(x) = \frac{1}{x\sigma_t\sqrt{2\pi}}\exp\left(-\frac{(\ln x - \mu_t)^2}{2\sigma_t^2}\right) \tag{6}$$

where $\mu_t = E\{\ln(\phi_{t,rms})\}$ and $\sigma_t = \text{std}\{\ln(\phi_{t,rms})\}$. The term $E\{\cdot\}$ is the expectation operation and the acronym std stands for the standard deviation of a random variable. We recall herein that the lognormal distribution is also adopted by different standardisation bodies, such as the 3GPP (3rd Generation Partnership Project) and COST 273, as an effective means to model global azimuth spreads [4, 27].

From Figs. 4 and 5, we can clearly observe the excellent fit for the AoA spread while the AoD spread exhibits a slight deviation from the lognormal cdf, especially for the NLoS case. This can be attributed to the so-called transmit bimodal angular distribution which occurs at all Tx locations close to the Rx (locations 13–16) and violates the single mode assumption that lies behind the power normality on the exponential scale. In physical terms, the obstructed LoS component and the back-wall reflections contribute to the creation of two separate regions (modes) across the transmit spatial domain; this phenomenon is clearly illustrated in Fig. 6 where an AoD histogram for location 14D3 has been plotted. At the Rx though, due to the highly cluttered environment in which it is situated, this effect becomes very weak and therefore the AoAs are more evenly distributed across the azimuth domain.

5.2 Correlation between the angular domains

A correlation study was also performed in order to investigate whether the mechanisms leading to spatial dispersion at the two ends are similar. The spatial correlation coefficient was calculated for each measurement scenario according to

$$\rho_{\phi_t,\phi_r} = \left|\frac{\sum_{p=1}^{P} (\phi_{t,rms}(p) - \overline{\phi}_{t,rms})(\phi_{r,rms}(p) - \overline{\phi}_{r,rms})}{\sqrt{\sum_{p=1}^{P} (\phi_{t,rms}(p) - \overline{\phi}_{t,rms})^2 \sum_{p=1}^{P} (\phi_{r,rms}(p) - \overline{\phi}_{r,rms})^2}}\right|,$$
$$\rho_{\phi_t,\phi_r} \in [0, 1] \tag{7}$$

where $\overline{\phi}_{t,rms}$, $\overline{\phi}_{r,rms}$ are the average values of the transmit and receive azimuth spreads, respectively. All obtained values are shown in Table 1.

Analysis of the measurement results revealed a high correlation at LoS (17) and OLoS locations (13D1, 14D3, 23D3, 24D3) where the Tx–Rx distance is low and the Tx faces the Rx. (For illustrative purposes, the values obtained at LoS locations are depicted in heavy-gray coloured cells while the Tx facing the Rx cases in light-gray coloured cells). This is anticipated since the direct dominant component is followed by multiple reflections which all follow a similar route thereby leading to a high correlation. The dependency of the spatial domains in the LoS case can be regarded as a counterpart of the high correlation between the spatio-temporal domains (again under LoS conditions) as documented in [7, 14]. On the contrary, at

Table 1 Spatial characteristics at all Rx locations and orientations

Rx location	No. of clusters			$\bar{\phi}_{r,rms},^{\circ}$			$\bar{\phi}_{t,rms},^{\circ}$			ρ_{ϕ_t,ϕ_r}		
	D1	D2	D3	D1	D2	D3	D1	D2	D3	D1	D2	D3
1	4	6	5	21.9	44.2	26.2	23.3	21.2	22.5	0.13	0.17	0.36
2	6	6	7	21.0	46.9	29.8	28.6	23.7	19.7	0.08	0.35	0.57
3	5	8	7	15.3	42.3	44.4	28.3	23.3	30.3	0.17	0.21	0.11
4	5	8	8	30.4	50.2	26.2	26.3	26.2	19.6	0.27	0.01	0.58
5	6	7	6	11.4	45.2	35.0	32.3	27.4	26.9	0.25	0.11	0.23
6	6	7	7	40.1	40.8	29.5	28.1	24.8	23.9	0.42	0.19	0.48
7	6	7	9	34.2	39.9	27.5	31.3	24.8	23.3	0.06	0.52	0.56
9	7	8	8	50.8	33.9	27.8	31.1	25.1	26.1	0.21	0.26	0.21
10	8	6	10	21.4	52.6	37.3	20.3	17.2	17.5	0.52	0.30	0.12
12	7	7	8	43.4	19.1	19.5	17.9	17.0	15.7	0.23	0.14	0.32
13	7	7	7	11.6	54.6	50.1	17.0	45.6	31.8	0.61	0.22	0.25
14	7	8	7	27.2	47.1	13.0	45.3	51.2	33.8	0.53	0.05	0.51
15	7	7	6	29.8	37.0	27.8	40.6	47.8	42.5	0.33	0.03	0.15
16	9	6	7	45.1	31.4	23.6	47.1	48.5	49.3	0.42	0.16	0.18
17	9	5	6	13.0	35.2	31.4	14.9	11.0	10.2	0.65	0.42	0.47
18	7	7	9	56.8	49.0	30.3	15.4	12.4	16.3	0.35	0.66	0.40
19	4	10	4	26.5	51.5	31.1	14.5	15.6	11.2	0.58	0.37	0.63
20	5	7	7	42.6	34.3	23.3	25.8	22.6	27.2	0.11	0.48	0.12
21	10	9	4	33.9	43.2	21.3	22.9	27.8	26.0	0.03	0.33	0.34
22	5	9	9	43.3	47.6	30.1	22.6	26.2	24.6	0.14	0.15	0.12
23	9	8	9	40.3	43.5	26.1	21.1	25.4	23.7	0.33	0.03	0.70
24	7	6	4	40.8	39.4	15.2	33.6	29.3	28.2	0.23	0.31	0.79
25	5	7	3	34.1	46.9	21.2	34.0	39.6	38.1	0.38	0.17	0.22
26	5	8	8	40.8	37.1	24.0	31.8	37.9	39.1	0.41	0.04	0.34

The heavy and light-gray colored cells correspond to LoS and OLoS locations, respectively

the vast majority of NLoS locations the dominant path vanishes and the degree of correlation is relatively low; under these circumstances, the propagation mechanisms have become far more complex (multiple-order reflection, diffraction and scattering) and the impinging paths follow different routes reducing the dependency of the two domains. As far as the mean azimuth spread is concerned, a number of interesting conclusions have been drawn. Firstly, we note that the LoS and OLoS locations exhibit the lowest dispersion, indicating a lower spatial decorrelation, as the dominant paths mask the scattered waves making them lie within the noise region; that is, the lower power paths are not observable and hence did not contribute to the global azimuth spread. The Rx locations in the vicinity of the outer wall (such as 9D1, 12D1,

16D1, 18D1, 18D2, 20D1, 22D1, 22D2, 25D2) yield very high values of AoA spread because of the weak high-order waves which bounce off the surrounding walls.

For the AoD dispersion, its large values at locations 14–16 are due to the bimodal energy distribution as alluded to in Section 5.1. In general, the receive azimuth spread is higher than the transmit spread at 51 out of the 72 considered scenarios (71.8% of the cases). Likewise, the AoA spread ranges between 11 and 56 degrees whereas the AoD spread between 10 and 51 degrees. One explanation suggests that the transmitted energy is confined within a region around the direct Tx–Rx path while the received multipath activity is spread over the whole azimuth domain. This means that the transmitted waves create a
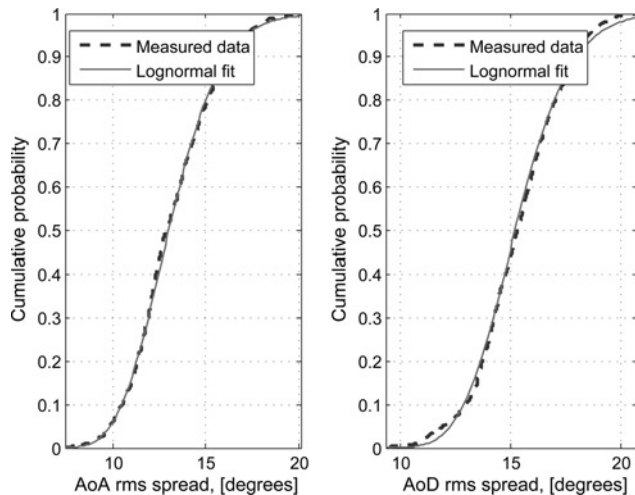
Figure 4 *Empirical azimuth rms spreads and best fit lognormal distributions for a LoS location (17D1)*

Figure 6 *Histogram of AoDs for location 14D3 showing the bimodal distribution across the transmit azimuth domain*

single or at most two clusters under the bimodal conditions and hence the values of the transmit spread are normally lower than those of the receive spread. In any case though, the obtained values are well above the ones reported in the corresponding literature from measurements at a base station mounted above rooftops [10, 11]; this is a direct consequence of the low antenna heights and closer proximity of local scatterers.

5.3 Ergodic capacity

From an information theory point of view, the performance of MIMO systems is commonly quantified with regard to their ergodic (or average) channel capacity. The capacity calculation includes the removal of the path-loss effects and hence the measured ensemble should be normalised so that the constraint $E\{\|\boldsymbol{H}\|_F^2\} = MN$ is fulfilled, where $\|\cdot\|_F$ corresponds to the Frobenius norm. Assuming perfect
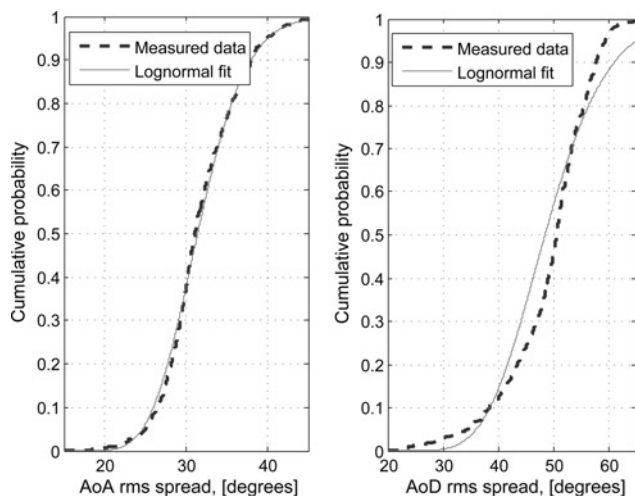
channel state information at the Rx but no knowledge at the Tx, the ergodic capacity (bits/s/Hz) is given by

$$\overline{C} = E\left\{\log_2\left(\det\left(\boldsymbol{I}_M + \frac{\rho}{N}\boldsymbol{H}\boldsymbol{H}^{\mathrm{H}}\right)\right)\right\} \tag{8}$$

where $\boldsymbol{I}_M$ is the $M \times M$ identity matrix and ρ denotes the system SNR per receiver branch [1]. The latter was set equal to 20 dB so that the system SNR is well below the measurement SNR values.

In Figs. 7 and 8, the ergodic capacity has been plotted against the spatial parameters of interest, these are, the azimuth spreads along with the correlation coefficient between them. Normally, low angular spreads cause a systematic decrease in MIMO capacity since they diminish the advantages of multipath propagation causing the rank-deficiency of the channel matrix [26]. Clearly, a consistent observation can be made for the measured data set under investigation; the effects of azimuth spread on capacity are

Figure 5 *Empirical azimuth rms spreads and best fit lognormal distributions for a NLoS location close to the Rx (16D2)*
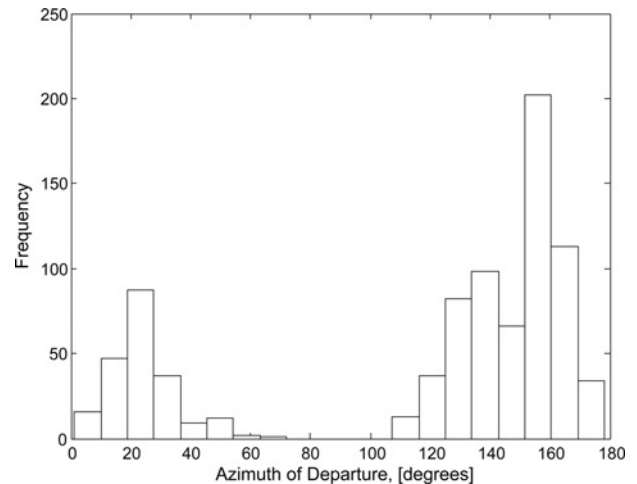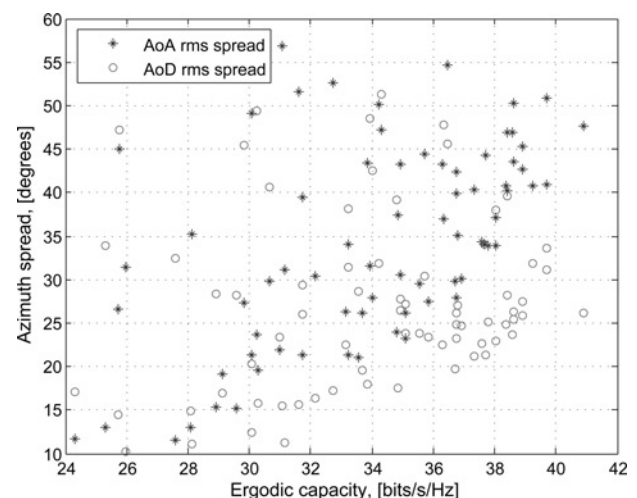

Figure 7 *Ergodic capacity as a function of the mean rms azimuth spreads $\bar{\phi}_{t,rms}$ and $\bar{\phi}_{r,rms}$*
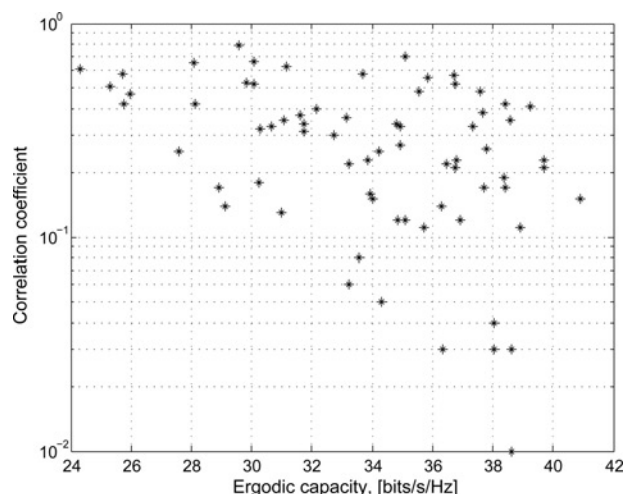
Figure 8 *Ergodic capacity as a function of the correlation coefficient ρ_{ϕ_t,ϕ_r} between the rms azimuth spreads*

more pronounced at the receive side where $\overline{\phi}_{r,\mathrm{rms}}$ and $\overline{C}$ behave in a more correlated way than $\overline{\phi}_{t,\mathrm{rms}}$ and $\overline{C}$ do. From a statistical viewpoint, the correlation between $\overline{\phi}_{r,\mathrm{rms}}$ and $\overline{C}$ is 0.5518 while between $\overline{\phi}_{t,\mathrm{rms}}$ and $\overline{C}$ is 0.1574. This trend may be attributed to the fact that the values of transmit azimuth spreads are slightly misleading due to either the bimodal distribution or near-field scattering effects which artificially increase them. This means that high transmit spreads are not always indicative of high multipath activity and therefore do not always lead to larger MIMO capacities. Similarly, an increase in dependency between the spatial domains leads to a decrease in the ergodic capacity. The relatively small number of deviations from this general trend can be attributed to strong OLoS components which raise the total received power level but, at the same time, contribute to a high degree of correlation. For practical systems, large angular spreads have a beneficial effect on MIMO capacity by enriching the SM potential (higher number of orthogonal subchannels) while independence of the two angular domains leads to an improvement in the spatial diversity of the MIMO link (high reliability).

6 Conclusion

In this paper, our main goal has been twofold. Firstly, we identified the dominant MPCs of an indoor MIMO channel by means of their angular characteristics in order to get a physical interpretation of the underlying propagation mechanisms. Secondly, we categorised both spatial domains with regard to the degree of dispersion and correlation between them. Lower dispersion and higher correlation occur when a LoS is present or when the Tx faces the Rx and the distance between them is low (OLoS propagation) while for NLoS Rx locations, the dispersion is larger and in turn the two spatial domains are rather decorrelated. The transmit bimodal angular distribution is another interesting phenomenon that artificially increases the AoD spread at

Rx locations close to the Tx. We eventually verified the common belief that high angular spreads contribute to high MIMO capacities while the independence of the two azimuth domains seems to have a positive impact on capacity performance. Finally, it should be pointed out that the results of the present study are general enough to allow description of Wireless Local Area Networks (WLANs) and peer-to-peer communications operating in the 5-GHz band.

7 Acknowledgments

8 References

[1] FOSCHINI G.J., GANS M.J.: 'On limits of wireless communication in a fading environment when using multiple antennas', *Wirel. Pers. Commun.*, 1998, **6**, (3), pp. 311–335

[2] STEINBAUER M., MOLISCH A.F., BONEK E.: 'The double-directional radio channel', *IEEE Antennas Propag. Mag.*, 2001, **43**, (4), pp. 51–63

[3] HAMPICKE D., SCHNEIDER C., LANDMANN M., RICHTER A., SOMMERKORN G., THOMA R.S.: 'Measurement-based simulation of mobile radio channels with multiple antennas using a directional parametric data model'. Proc. IEEE Vehicular Technology Conf. (VTC), Atlantic City, NJ, USA, 2001, vol. 2, pp. 1073–1077

[4] CORREIA L, (ED.): 'COST 273 final report: Towards mobile broadband multimedia networks' (Elsevier, 2006)

[5] SALEH A.A.M., VALENZUELA R.A.: 'A statistical model for indoor multipath propagation', *IEEE J. Sel. Areas Commun.*, 1987, **5**, (2), pp. 128–137

[6] SPENCER Q.H., JEFFS B.D., JENSEN M.A., SWINDLEHURST A.L.: 'Modeling the statistical time and angle of arrival characteristics of an indoor multipath channel', *IEEE J. Sel. Areas Commun.*, 2000, **18**, (3), pp. 347–359

[7] CHONG C.C., TAN C.M., LAURENSON D.I., MCLAUGHLIN S., BEACH M.A., NIX A.R.: 'A new wideband spatio-temporal channel model for 5-GHz band WLAN systems', *IEEE J. Sel. Areas Commun.*, 2003, **21**, (2), pp. 139–150

[8] CZINK N., YIN X., ÖZCELIK H., HERDIN M., BONEK E., FLEURY B.: 'Cluster characteristics in a MIMO indoor propagation environment', *IEEE Trans. Wirel. Commun.*, 2007, **6**, (4), pp. 1465–1475

[9] PEDERSEN K.I., MOGENSEN P.E., FLEURY B.H.: 'A stochastic model of the temporal and azimuthal dispersion seen at the base station in outdoor propagation environments', *IEEE Trans. Veh. Technol.*, 2000, **49**, (2), pp. 437–447

[10] ALGANS A., PEDERSEN K.I., MOGENSEN P.E.: 'Experimental analysis of the joint statistical properties of azimuth spread, delay spread, and shadow fading', *IEEE J. Sel. Areas Commun.*, 2002, **20**, (3), pp. 523–531

[11] FOO S.E., TAN C.M., BEACH M.A.: 'Spatial temporal characterization of UTRA FDD channels at the user equipment'. Proc. IEEE Vehicular Technology Conf. (VTC), April 2003, vol. 2, pp. 793–797

[12] TAN C.M., NIX A.R., BEACH M.A.: 'Dynamic spatial-temporal propagation measurement and super-resolution channel characterisation at 5.2 GHz in a corridor environment'. Proc. IEEE Vehicular Technology Conf. (VTC), Vancouver, Canada, September 2002, pp. 797–801

[13] CHONG C.C., LAURENSON D.I., MCLAUGHLIN S.: 'Spatio-temporal correlation properties for the 5.2-GHz indoor propagation environments', *IEEE Antenna Wirel. Propag. Lett.*, 2003, **2**, (8), pp. 114–117

[14] WYNE S., CZINK N., KAREDAL J., ALMERS P., TUFVESSON F., MOLISCH A.: 'A cluster-based analysis of outdoor-to-indoor office MIMO measurements at 5.2 GHz'. Proc. IEEE Vehicular Technology Conf. (VTC), Montreal, Kanada, September 2006, pp. 1–5

[15] THOMÄ R.S., HAMPICKE D., RICHTER A., ET AL.: 'Identification of time-variant directional mobile radio channels', *IEEE Trans. Instrum. Meas.*, 2000, **49**, (2), pp. 357–364

[16] WEICHSELBERGER W.: 'Spatial structure of multiple antenna tadio channels: a signal processing wiewpoint', PhD Thesis, Technical University of Vienna, 2003

[17] ÖZCELIK H.: 'Indoor MIMO channel models'. PhD Thesis, Technical University of Vienna, 2004

[18] PENSEL K., NOSSEK J.A.: 'Uplink and downlink calibration of an antenna array in a mobile communication system', COST 259 Technical Document, TD(97)55, Lisbon, Portugal, September 1997

[19] MATTHAIOU M., RAZAVI-GHODS N., LAURENSON D.I., SALOUS S.: 'Characterization of an indoor MIMO channel in frequency domain using the 3D-SAGE algorithm'. Proc. IEEE Int. Conf. Communications (ICC), Glasgow, UK, June 2007, pp. 5868–5872

[20] FESSLER J.A., HERO A.O.: 'Space-alternating generalized expectation-maximization algorithm', *IEEE Trans. Signal Process*, 1994, **42**, (10), pp. 2664–2677

[21] CHONG C.C., LAURENSON D.I., TAN C.M., MCLAUGHLIN S., BEACH M.A., NIX A.R.: 'Joint detection estimation of directional channel parameters using the 2-D frequency domain SAGE algorithm with serial interference cancellation'. Proc. IEEE Int. Conf. Communications (ICC), New York, USA, April 2002, vol. 2, pp. 906–910

[22] JAIN A.K., DUBES R.C.: 'Algorithms for Clustering data' (Prentice-Hall, Englewood Cliffs, NJ, USA, 1988)

[23] HALL P., SHEATHER S.J., JONES M.C., MARRON J.S.: 'On optimal data-based bandwidth selection in kernel density estimation', *Biometrika*, 1991, **78**, (2), pp. 263–269

[24] SILVERMAN B.W.: 'Density estimation for statistics and data analysis' (Chapman and Hall, London, UK 1986)

[25] Ihler A.: 'Kernel density estimation toolbox for MATLAB', http://ssg.mit.edu/ihler/code/kde.shtml, accessed October 2007

[26] SHIU D.S., FOSCHINI G.J., GANS M.J., KAHN J.M.: 'Fading correlation and its effects on the capacity of multielement antenna systems', *IEEE Trans. Commun.*, 2000, **48**, (3), pp. 502–513

[27] 3GPP - 3GPP2 Spatial Channel Model Ad-hoc Group, 'Spatial channel model for MIMO systems', technical report 3GPP and 3GPP2; download at http://www.3gpp.org, accessed September 2007